DOI: 10.13009/EUCASS2023-916
Aerospace Europe Conference 2023 – 10TH EUCASS – 9TH CEAS

Heat Transfer Assessment in a Vaporizing Liquid Microthruster undergoing Dual Heating Control

Donato Fontanarosa[1], *Guido Marseglia*[2], *Maria Assunta Signore*[3], *Angelica Maria Toscano*[2], *Johan Steelant*[4], *Maria Grazia De Giorgi*[2†], *Luca Francioso*[3] *and Maria Rosaria Vetrano*[1]

[1]*KU Leuven, Department of Mechanical Engineering, Division of Applied Mechanics and Energy Conversion (TME), B-3001 Leuven, Belgium*
[2]*Dept. of Engineering for Innovation, University of Salento, via per Monteroni, Lecce I-73100, Italy*
[3]*Institute for Microelectronics and Microsystems IMM-CNR, Via per Monteroni Campus Ecotekne, Lecce, Italy*
[4]*Flight Vehicles and Aerothermodynamics Engineering Section, ESTEC-ESA, Keplerlaan 1, 2200AG Noordwijk, the Netherlands*

mariagrazia.degiorgi@unisalento.it
[†]Corresponding author(s)

Abstract

In the present work, a new VLM design is proposed to ensure a safer and more efficient heat transfer of high-energy from solid walls to fluid. In this regard, an innovative approach is introduced to separate the boiling and overheating processes by implementing two distinct heating chambers. A quasi-1D steady-state numerical model has been developed to solve the flow into the VLM at constant heat flux boundary conditions, allowing for a preliminary performance assessment of dual heating control. Thus, in-depth insights derived from both the experimental assessment and numerical analysis are comprehensively discussed and presented, highlighting their relevance and significance in understanding the heat transfer process.the most relevant insights are discussed together with the numerical analysis.

1. Introduction

The recent advancements in micro-electro-mechanical systems (MEMS) technology have enabled the development of secondary micropropulsion systems for small satellites (total mass < 10 kg), used for Earth and Deep Space observation, and the simplicity of the concept and the use of lighter and smaller propellant tanks make vaporizing liquid microthrusters (VLMs) a promising solution. The first water-fuelled MEMS-based VLM studies date back to the end of the ′90s with Mueller′s works[1,2],[3] followed by continuous and independent research activities involving different configurations, materials, and manufacturing technologies.[4] For instance, concerning the silicon technology, Mukejee *et al.*[5] first used wet anisotropic etching, while Maurya *et al.*[6] designed and fabricated a silicon-based VLM with an integrated micro-heater and, later, Kundu *et al.*[7] developed a new device design using two heaters integrated on the silicon substrate to ensure uniform heating of the silicon structures. Instead, Ye *et al.*[8] applied an electric pulse producing an impulse bit of about 2 µN s. More recently, Silva *et al.*[9] developed a VLM with embedded molybdenum heaters, which was integrated into the attitude control system of a real research program for CubeSats and PocketQubes. Liu *et al.*[10,11] developed and tested two VLM concepts using induction heating, characterized by tubular and planar geometry. Recently, novel concepts of capillary-fed MEMS microthrusters have been proposed in *et al.*[12] and Pugia *et al.*[13],[14] which exploit the localized evaporation of a thin water film obtained using micro-engineered surfaces. Regardless of their design, the common experimental evidence is that VLMs can provide thrust force ranging between 0.1 and 10 mN with a nominal specific impulse between 50 s and 100 s using water as a green propellant.[15] However, the technology readiness level of such devices is still below 3 mainly due to the complexity of the vaporization process. In fact, in VLMs the water flow is typically heated to temperatures higher than its boiling point, resulting in an inherently unstable behavior due to detrimental flow boiling instabilities. This reduces the VLM′s lifetime and significantly impairs its nominal performance due to low thermal efficiency and thrust unsteadiness.[16] They usually occur inside the inlet and heating chambers, causing pressure-temperature-mass flow rate oscillations, dramatically affecting the expansion process into the micronozzle and, hence, the propulsive performance. In this regard, Chen *et al.*[17] first characterized the

DOI: 10.13009/EUCASS2023-916

two-phase flow in a single-channel silicon-based VLM, observing four different flow patterns, i.e., snake flow, vapour-droplet flow, vapour-droplet-jet flow, and vapour flow. They observed that even the snake flow pattern could lead to the device failure of the micro-thruster when the device was not properly heated. Instead, Cen and Xu[18] first fabricated a MEMS-based VLM made by parallel microchannels and clearly detected the inception of parallel channel flow boiling instabilities due to explosive boiling. Recently, Kwan *et al.*[19] developed a VLM operating above the critical heat flux condition in the Leidenfrost boiling regime.

To control such flow boiling instability, in the framework of an ESA OSIP project we designed and manufactured a MEMS-based VLM using a parallel microchannels system as a heating chamber.[20] The device has a sandwich structure that is created by using anisotropic wet etching on a silicon substrate, while a glass substrate is fixed onto the silicon pad by adhesive bonding. Additionally, a set of thermistors and vapour quality capacitive sensors have been designed to equip the microthruster with local sensing capabilities. In our previous investigations,[21,22] we have found that the optimization of the heat transfer process and, as a result, the maximization of the propulsive performance, is limited when using one single heating system and geometry. This is due to the high-density ratio of water, which makes it impossible to achieve both a high and efficient energy transfer and device safety simultaneously: to transfer high energy from solid walls to the fluid, we need to operate at device temperatures well above the threshold tolerated by adhesive bonding. To overcome this design limit, a new VLM design is proposed for a safer and more efficient high-energy transfer from solid walls to fluid. In such a new design, two independent heating chambers actively separate the boiling and overheating processes. In this regard, a quasi-1D steady-state numerical model has been developed to solve the flow into the VLM at constant heat flux boundary conditions, which is described in Section 2. Therefore, an experimental evidence of the heat transfer process on a real device undergoing dual heating control is provided first, followed by the description of the modified design together with the numerical assessment of the steady-state dual heating process (Section 3). Finally, the most relevant insights are discussed and summarized in Section 4.

2. Methods and Methodologies

2.1 Quasi-1D steady-state numerical model of a VLM

The generic schematics of a VLM consists of three parts: the inlet chamber or plenum through which the propellant is fed, the heating chamber where the propellant is vaporized, and the convergent-divergent micronozzle, which accelerates the superheated vapor flow to supersonic velocities. The proposed analytical model is a modification of the one proposed in De Giorgi and Fontanarosa,[23] to which the authors refer for a more detailed description of the main governing equations. It couples the steady-state solution of the heating process into the heating chamber with the solution of the expansion process into the micronozzle, where the former determines the flow conditions at the micronozzle entrance and the second one points to estimate the thruster performance taking into account the mass flow rate loss caused by the boundary layer growth inside the micronozzle.

A 1D steady-state boiling model describes the behavior of the liquid-vapor flow inside the inlet and the heating chambers of the microthruster. It is based on the assumptions of thin film flow :[24] Newtonian flow with no slip condition at the inner walls, inertia and other body forces such as the gravity negligible compared to pressure and viscous forces, with instantaneous velocity changes. The fluid properties are averaged over the entire cross-section by supposing the homogeneous mixture of liquid and vapor in thermodynamic equilibrium with properties retrieved using the toolbox CoolProp.[25] Consequently, the generic mixture property $g(\cdot)$, marked by the subscript m, is function of the vapor quality x, and the corresponding saturated properties of liquid and vapor phases (denoted by the subscripts l and v) as $g_m(\cdot) = x\ g_v(\cdot) + (1-x)\ g_l(\cdot)$. The heat flux $\dot{q}$ is related to the convective heat exchange driven by the heat transfer coefficient $h_b = Nu\frac{\kappa_{cond}}{D_h}$, where κ_{cond} is the local thermal conductivity coefficient of the fluid and D_h is the hydraulic diameter. Instead, the Nusselt number Nu is locally estimated based on the empirical correlations extrapolated by Tibiriç′a et al.[26] In particular, the heat transfer process is influenced by the establishment of the dry-out condition $x_{d/o}$ as reported in Eq. (1), which imposes a limit above which the behavior of the saturated liquid-vapor mixture approaches the dry vapor state:

$$x_{d/o} = \min(x_{incip}, x_{crit}, x_{dry,max}) \tag{1}$$

where $x_{dry,max}$ is an upper limit set equal to 0.95 as suggested by,[26] x_{incip} is the incipient dry-out vapor quality estimated as:

$$x_{incip} = 0.6827\ Eo^{0.07395}\ X_\rho^{0.07149}\ Bo^{0.04786}\ (1-x_{TD})^{-0.3378} \tag{2}$$

In Eq. (2), $X_\rho = \frac{\rho_l}{\rho_v}$ is liquid-to-vapor density ratio, $Eo = \frac{g_0(\rho_l-\rho_v)\ D_h^2}{\sigma}$ is the Eötvös number and $Bo = \frac{\dot{q}}{h_L G}$ is the boiling number. x_{TD} is the thermodynamic vapor quality of the water-steam mixture at the entrance of the inlet chamber, and

DOI: 10.13009/EUCASS2023-916

x_{crit} is the vapor quality corresponding to the critical heat flux condition (CHF), resulting from:

$$x_{crit} = 4\ Bo \left[4.124\ Bo\ We^{0.1625}\ X_{\rho}^{0.05981}\ La^{0.07142}\ (1 - x_{TD})^{-0.8809}\right]^{-1.4632} + x_{TD} \tag{3}$$

where $Re = \frac{GD_h}{\mu}$ is the Reynolds number, $La = \frac{\rho_l \sigma D_h}{\mu}$ is the Laplace number, $Fr = \frac{G^2}{\rho_l g_0 D_h}$ is the Froud number, $We = \frac{G^2 D_h}{\sigma \rho_l}$ is the Weber number and $Pr = \frac{c_p \mu}{\kappa_{cond}}$ is the Prandtl number. Finally, the local heat transfer coefficient is estimated as in Eq. (4):

$$h_b = \begin{cases} \frac{Nu(x)\ \kappa_{cond}}{D_h} & \text{if } x < x_{d/o} \\ \frac{Nu(x)\ \kappa_{cond}}{D_h} - 0.5 \left[\frac{Nu(x)\ \kappa_{cond}}{D_h} - h_{b,DB}\right] \frac{(x - x_{d/o})}{(1 - x_{d/o})} & \text{if } x \geq x_{d/o} \end{cases} \tag{4}$$

Instead, the local Nusselt number and the Dittus-Boelter superheated vapor relation are defined in Eqs. (5) and (6):

$$Nu(x) = \begin{cases} 0.68\ Pr^{0.5414}\ La^{0.1942}\ Re^{0.5873}\ (1 - x)^{-0.2446}\ Bo^{0.3544} & \text{if } x < x_{d/o} \\ 0.68\ Pr^{0.5414}\ La^{0.1942}\ Re^{0.5873}\ (1 - x_{d/o})^{-0.2446}\ Bo^{0.3544} & \text{if } x \geq x_{d/o} \end{cases} \tag{5}$$

$$h_{b,DB} = 0.023\ \frac{\kappa_{v,cond}}{D_h}\ Re_v^{0.8}\ Pr_v^{1/3} \tag{6}$$

where Re_v and Pr_v respectively are the local Reynolds and Prandtl numbers of the vapor phase. The operational range of validity of the experimental correlations by[26] is reported in Tab. 1.

Table 1: Operational ranges of validity of the experimental correlations by.[26]

Quantity	Range of validity
Fluids	water, R12, R22, R123, R134a, R236fa, R245fa, R1234ze(E), R1234yf, R744 (Carbon Dioxide), R290 (Propane), R410a, R600a and nitrogen
We^*	$[1 \times 10^{-1} \div 2 \times 10^5]$
La^*	[46 600 ÷ 3 131 000]
Re^*	[120 ÷ 14 600]
Bo^*	$[4.6 \times 10^{-5} \div 2.5 \times 10^{-3}]$
Pr^*	[0.9 ÷ 6.6]
$x_{TD}{}^*$	[−0.6 ÷ 0.15]
$\frac{\texttt{channel length}}{\texttt{channel diameter}}$	[20 ÷ 500]
X_ρ	[6.5 ÷ 129 000]

* evaluated at the entrance of the inlet chamber.

It is useful specifying the symbols used in defining the dimensionless numbers cited above: G is mass flow rate per unit cross section area; g_0 is the gravitational acceleration; h_L is the latent heat of vaporization; c_p and c_v are the specific heats at constant pressure and constant volume, respectively; μ is the dynamic viscosity; ρ is the fluid density and σ is the surface tension.

Concerning the solution of the supersonic expansion process of the vapor flow through the micronozzle, the ideal propulsive performances (thrust force F_{IRT} and specific impulse $I_{sp,IRT}$) are first computed from the ideal rocket theory (IRT)[27] as the sum of two contributions, i.e., the momentum and the pressure thrust, denoted by the subscripts j and p:

$$F_{IRT} = F_{j,IRT} + F_{p,IRT} = \dot{m}_{IRT}\ u_{exit,IRT} + (p_{exit,IRT} - p_{amb})\ A_{exit} \tag{7}$$

$$I_{sp,IRT} = \frac{F_{IRT}}{\dot{m}_{IRT}\ g_0} = \frac{u_{eff}}{g_0} \tag{8}$$

In the equations above u_{eff} is the effective exhaust velocity which takes into account both thrust terms, $\dot{m}_{IRT}$ is the maximum ideal mass flow rate, $p_{exit,IRT}$ and $u_{exit,IRT}$ are the ideal static pressure flow velocity at the exit section, A_{exit} is the exit area of the micronozzle, and $g_0 = 9.81\ \mathrm{ms}^{-2}$ is the starndard gravitational acceleration. The establishment of the boundary layer at the nozzle throat and along the divergent section at the micro-scale strongly affects the efficiency expansion process, and the actual thrust decreases due to losses of both mass flow rate and exit velocity, as in Eq. (9):

$$F_{act} = \dot{m}_{act} u_{act} = (C_d\ \dot{m}_{IRT})\ (\eta_u\ u_{IRT}) = (C_d \eta_u)\ \dot{m}_{IRT} u_{IRT} = \xi_n F_{IRT} \tag{9}$$

where C_d is the discharge coefficient, η_u is the I_{sp}-efficiency, and $\xi_n = C_d\ \eta_u$ defines the global propulsive efficiency, better known as nozzle quality. As highlighted in Eq. (9), the nozzle quality quantifies the total performance losses due to the boundary layer thickness inside the micronozzle.

DOI: 10.13009/EUCASS2023-916

Therefore, the ideal performance are corrected by considering two loss factors: the discharge coefficient C_d and the I_{sp}-efficiency. The former quantifies the mass flow rate losses due to the development of the boundary layer at the throat section as follows:[28]

$$C_d = C_d\left(\frac{r_c}{0.5\ W^*}, \gamma, Re^*\right) = \left[\frac{r_c + 0.05\ (0.5W^*)}{r_c + 0.75\ (0.5W^*)}\right]^{0.019} \left\{1 - \left[\frac{r_c + 0.10\ (0.5W^*)}{(0.5W^*)}\right]^{0.21} \left(\frac{1}{Re^*}\right)^{0.5} f(\gamma)\right\} \quad (10)$$

where $\gamma = c_p/c_v$ is the specific heat ratio, Re^* is the Reynolds number at the throat section, r_c and W^* are the radius of curvature and the width of the throat, and $f(\gamma) \simeq 0.97 + 0.86\gamma$. As specified in,[28] the operational range of validity of the correlation (10) is $0 \leq r_c/W^* \leq 20$ and $50 \leq Re^* \leq 1 \times 10^5$. However, the difference between the inviscid and the viscous velocity inside the boundary layer leads to a reduction of the momentum ΔJ too. Thus, ΔJ has been derived[29] for a planar nozzle as a function of the compressible displacement δ^* and the momentum thicknesses θ:

$$\Delta J = \dot{m}_{act} u_{exit,IRT} \left(\frac{2\delta^*}{W_{exit}}\right)\left(1 + \frac{\theta}{\delta^*}\right) = \dot{m}_{act}\ \Delta u_{exit} \quad (11)$$

Concerning the I_{sp}-efficiency, it quantifies the momentum losses due to the viscous forces acting during the expansion process into the divergent section as follows:

$$\eta_u = \frac{u_{exit,act}}{u_{exit,IRT}} = \frac{u_{exit,IRT} - \Delta u_{exit}}{u_{exit,IRT}} = 1 - \left(\frac{2\delta^*}{W_{exit}}\right)\left(1 + \frac{\theta}{\delta^*}\right) \quad (12)$$

In the equation above, δ^* and θ depend on the Reynolds number and the Mach number at the exit, namely Re_{exit} and M_{exit}, which relate to the incompressible thicknesses as follows:[30]

$$S_{\delta^*} = \frac{\delta^*}{\theta} = \bar{S}\ (1 + 0.113M_{exit}^2) + 0.290M_{exit}^2 \quad (13)$$

$$\theta = \bar{\theta}\left\{1 - \frac{0.92M_{exit}^2}{7.09 + M_{exit}^2} \tanh[1.49(\bar{S} - 0.9)]\right\} \quad (14)$$

where S_{δ^*} is the compressible shape factor, $\bar{\delta^*}$ and $\bar{\theta}$ are respectively the incompressible displacement and momentum thicknesses, and $\bar{S} = \bar{\delta^*}/\bar{\theta}$ is the incompressible shape factor. The Eqs. (15), (16) and (17) proposed by Çengel and Cimbala[31] for turbulent flows are used to estimate $\bar{\theta}$ and $\bar{S}$, as follows:

$$\frac{\bar{\delta^*}}{L} = \frac{0.048}{Re_{exit}^{1/5}} \quad (15)$$

$$\frac{\bar{\theta}}{L} = \frac{0.037}{Re_{exit}^{1/5}} \quad (16)$$

$$\bar{S} = \frac{0.048}{0.037} = 1.2973 \quad (17)$$

where L is the slanted length of the expander.

2.2 Solution procedure

The grid step Δs has been set to 5×10^{-7} m, while the time step is estimated by considering the cell-centered flow velocity u as $\Delta t = \frac{\Delta s}{u}$. The solution procedure of the proposed model is iterative and based on a two-cycle criterion, as described in De Giorgi and Fontanarosa.[23] The first cycle forwardly solves the two-phase flow from the entrance to the exit of the heating region. The initialization of the mass flow rate is based on the hypothesis of chocked micronozzle, using the desired fluid temperature at the micronozzle entrance $T_{fluid,exit}$ and p_i. The Nusselt number is set constant and equal to 4.96 as suggested by Bejan.[32] A constant heat flux profile along the flow direction is also assigned and the two-phase flow is solved producing the flow conditions at the micronozzle entrance. Hence, the 0D model of real nozzle previously described compute the mass flow rate losses and the error between the corrected mass flow rate with the old one, the mass flow rate is updated before to start a new computational loop, until convergence is reached on the mass flow rate based on a residual tolerance of 0.01. The convergence on the first cycle leads to the estimation of the wall temperature profile T_{wall}, which is set as a boundary conditions for the second heat-flux based computational cycle. This last one is initialised by estimating the boiling number Bo and the other dimensionless numbers used in the

DOI: 10.13009/EUCASS2023-916

experimental correlation by Tibiriç'a *et al.*[26] based on the average heat flux $\dot{q}_0$. This ensures stability in the solution of the second and most important cycle, which is constructed using the empirical relations presented in the previous section. Therefore, the two-phase flow inside the heating region is first solved based on the local estimation of the Nusselt number. Hence, a new value of the average heat flux is estimated and a correction step is introduced on it, based on a residual tolerance of 0.001. Once convergence is reached on the average heat flux, the solution of the gas flow inside the micronozzle is computed starting from the fluid state predicted at the exit of the microchannel in combination with the 0D model of real nozzle previously described. The latter leads to the corrected mass flow rate at the end of each cycle loop. Thus, similarly to the first cycle, the mass flow rate correction is performed based on a residual tolerance of 0.01.

3. Results and discussion

3.1 Dual heating: original design and experimental evidence

The first VLM has been designed and manufactured by the Institute for Micro-electronics and Micro-systems of the Italian National Research Council (CNR-IMM), in collaboration with the Aerospace Propulsion group of the University of Salento (Italy) and the Heat and Mass Transfer group of the KU Leuven (Belgium). The original geometry consists of a long inlet chamber to easily accomodate an injection needle 33G, 8 parallel microchannels of 9 mm length as a heating chamber, and a tronco-conical planar micronozzle. The overall etching depth is equal to 260 µm. The manufacturing process involved reactive ion etching, plasma-enhanced chemical vapour deposition, adhesive bonding, micro-alignment, and micro-machining. The final VLM has a stacked configuration consisting of a silicon substrate with fluidic structures and a borosilicate glass cover lid, and a specially patterned glue layer binds the silicon and glass substrates and ensures fluid tightness. The device has been equipped with 7 resistance temperature detectors (RTDs), two arrays of in-channel capacitive void fraction sensors (VFSs), and in-channel low-power secondary resistive micro-heaters, and has been designed to operate with liquid water as the propellant at mass flow rate ranging between 2.0×10^{-6} kg/s and 7.0×10^{-6} kg/s and ultimate device temperature equal to 575 K. The ranges of nominal thrust and specific impulse range are 1 mN ÷ 10 mN and 90 s ÷ 110 s, respectively.

In our previous works,[20–22] the device feasibility using only the main heater has been assessed in constant voltage and actively controlled pulsed heating. In the present work, the secondary low-power heater was activated for the first time. In this regard, it is first worth providing the expected performance of the secondary heater coming from its design. The low-voltage/low-power secondary heating system is composed of eight thin film Pt microheaters (one per microchannel), each 3 mm long, 90 μm wide and 500 nm thick, as shown in Figure 1.

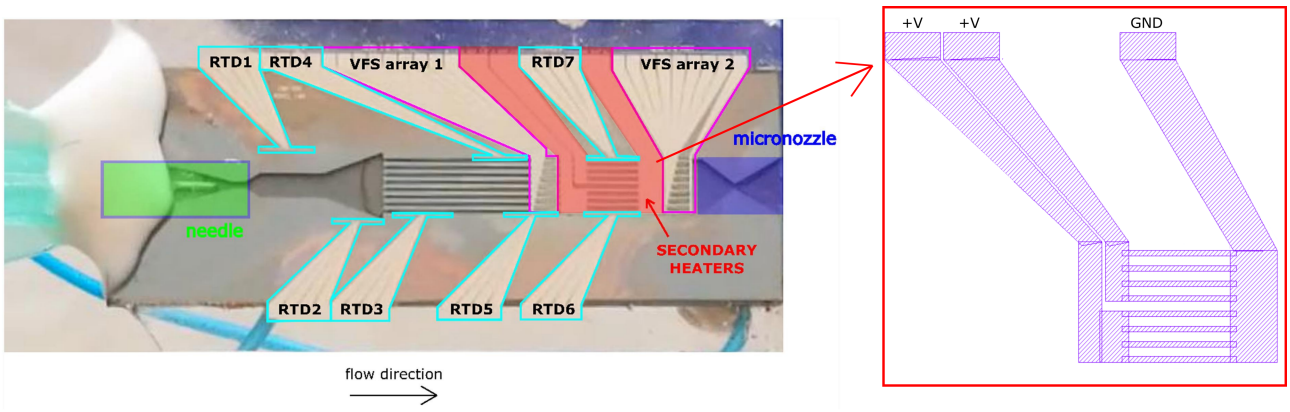

Figure 1: Schematics of the secondary micro-heaters and picture of the VLM.

The electrical resistivity of Pt as a function of the temperature is given by the following equation:

$$\rho_{Pt}(T) = \alpha_{ref,Pt}\rho_{ref,Pt}(T - T_{ref}) \tag{18}$$

where $T_{ref} = 293.15$ K is the reference temperature, the subscript *ref* refers to measurements at T_{ref}, while α_{Pt} represents the temperature coefficient of resistance and ρ_{Pt} is the electrical resistivity made of platinum (Pt). Therefore, the electrical resistance R_h calculations are based on $\rho_{ref,Pt} = 1.06 \times 10^{-7}\ \Omega$ m and $\alpha_{ref,Pt} = 0.00217$, which have been

DOI: 10.13009/EUCASS2023-916

experimentally retrieved by the CNR-IMM in previous tests, as follows:

$$R_h(T) = \rho_{Pt}(T)\frac{L_h}{H_h W_h} \tag{19}$$

where L_h, H_h and W_h represent length, thickness and width of the Pt conductor. Finally, the corresponding applied voltage V_{app} and electrical power P_{el} were computed by considering a maximum current density $j_{max} = 3.5\times10^9$ A/m^2 and the heater cross section $A_{cs,h} = H_h W_h$. The results are reported in Table 2 at different operating temperature T_w, i.e, 383 K, 453 K and 573 K.

Table 2: Preliminary design of the secondary heater: performance.

	T_w [K]		
	383	**453**	**573**
$\rho_{Pt}(T)$ [Ωm]	1.27×10^{-7}	1.43×10^{-7}	1.70×10^{-7}
$R_{h,sec}(T)$ [Ω]	8.45	9.52	11.4
V_{app} [V]	1.33	1.50	1.79
$P_{el,h}$ [W]	0.21	0.24	0.28
$P_{el,tot}$ [W]	1.68	1.89	2.25

The resistance of the secondary heater determines the power and heating capability, and its experimental characterization is given in Figure 2 showing the resistance curve. As expected, it is nonlinear and as the temperature rises due to the heating, the resistance also goes up. It is worth observing that at 3.5 V and 0.52 A, the device heated up at 110 °C, exhibiting an electrical resistance of about 6.73 Ω, which is quite close to the estimated one (8.45 Ω) shown in Tab. 2.

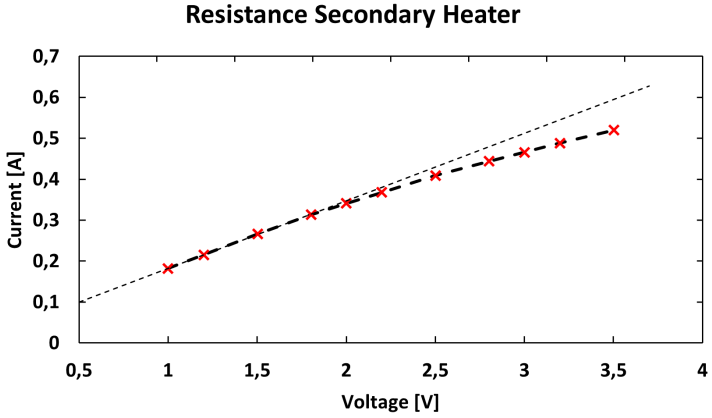

Figure 2: Resistance curve of the secondary heater.

After verification of the electrical performance of the secondary heaters, an experimental assessment of the effect of the secondary heating on the thermal performance of the VLM undergoing actively controlled pulsed heating on the main heater has been performed. Figure 3 shows the overall experimental setup, along with the apparatus required for injecting water into the VLM and the VLM itself equipped with external temperature sensors. The water feeding system consisted of a syringe pump (model NE-1000), plastic tubing, micro-fluidic valves, and fittings type Luer lock. The feeding pressure and temperature were measured using a relative pressure transducer Validyne DP15 (user calibrated in the relative pressure range 0 bar to 5 bar) and a K-type thermocouple, respectively. Both were located along the water feeding line before the VLM injection system. Concerning the heating system, the DC power supplier (model Agilent 5751a) was electrically connected to the main heater of the VLM through a metal-oxide-semiconductor field-effect transistor (MOSFET), model ICQUANZX, which operated a pulse width modulation (PWM) switch (maximum frequency equal to 20 kHz) allowing for a pulsed gating of the electrical feeding. The linear Hall effect current sensor HiLetgo ACS758LCB-050B-PFF-T (measuring range: 0 A to 50 A; response time: 16 µs; bandwidth: 120 kHz), placed between the MOSFET and the VLM heater, produced a voltage output which was directly acquired by the oscilloscope R&S RTB2004 (bandwidth: 300 MHz; 4 channels; sampling speed: 1.25 GS/s) using a voltage probe with attenuation factor 1:1. Two voltage probes (attenuation factor 1:1) located on the positive and negative leads of

DOI: 10.13009/EUCASS2023-916

the VLM heater were used to read the voltage applied on the oscilloscope, which thus synchronously read and wrote the applied voltage and the current signals across the VLM main heater. Mounted on a 4-slot chassis NI cDAQ-9174, the module NI-9401 controlled the MOSFET gate by generating the PWM signal. The actively controlled pulsed heating system applied to the main heater was linked to the device's temperature readings, which were obtained from two K-type thermocouples installed on the external surface of the quartz substrate. Figure 3(b) shows the final configuration of the VLM during testing: TC1 represents the thermocouple placed close to the inlet section (cold side), while TC2 represents the thermocouple placed close to the micronozzle entrance (hot side). Their signals were acquired using the data acquisition module NI-9211 (sampling speed: 14 Hz aggregate; 4 channels), mounted on the shared data acquisition chassis. This limited the speed of the resulting temperature controller to 4 Hz. The software development of the control system was performed using the toolbox Labview 2018 of National Instruments.

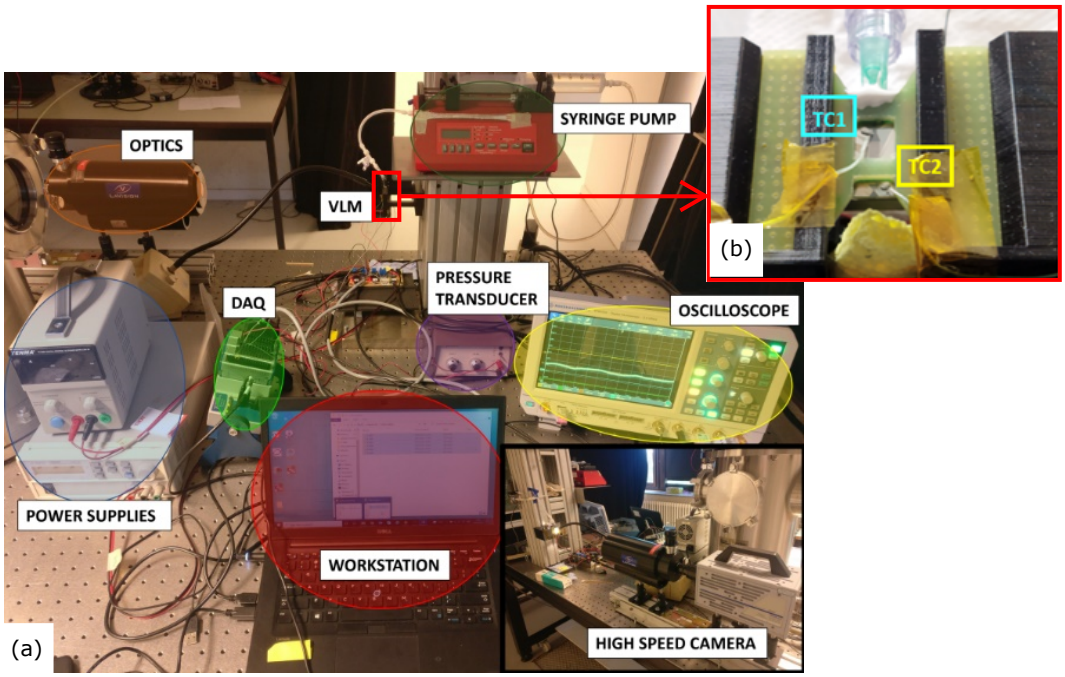

Figure 3: Experimental setup: (a) overall physical arrangement; (b) VLM configuration with thermocouples TC1 (VLM inlet, cold side) and TC2 (micronozzle entrance, hot side).

Some interesting effects have been observed when activating the secondary heater for the first time. In this regard, a manually tuned PI-D (proportional and integrative terms applied to the error; derivative term applied to the output) controller of TC1 triggered the main heating, while the secondary heater was manually switched on or off by the operator using a different power supply. Figure 4 shows the thermal response of the VLM, i.e., the temperatures at the nozzle and at the inlet, the setpoint temperature and the voltage of the secondary heater. From the moment the secondary heater is turned on to 4V, the temperature oscillations are significantly dampened and the inlet temperature decreases too. The latter is because the secondary heater provides part of the power, thus the PI-D controller reduces the power supplied to the primary heater, as shown in Figure 5 by the dropping duty cycle (from 0.7 to 0.6 when the secondary heater is on).

3.2 Dual heating: new device configuration and numerical assessment

The planar geometry of the new device is shown in Figure 6. By preserving the overall size of the previous design, the fluidic space has been rearranged as follows. The operating range of the mass flow rate has been scaled down in order to bring the nominal required power below 5 W and satisfy the available power requirement onboard CubeSats. As a result, a set of three parallel microchannels of 120 µm width and about 6 mm length define the boiling chamber. Upstream, the inlet chamber has been shortened to 1.2 mm to reduce the residence time of the flow and prevent from the undesired boiling incipience. In this regard, it is worth underlining that the aim of the inlet chamber is only equally distributing the flow into the microchannels. Furthermore, its geometry has been simplified to a weak convergent to compensate the small pressure losses and minimize the flow distortion before the microchannels entrance. This has been allowed by the modification of the water injection system: in fact, the 33G needle has been replaced

DOI: 10.13009/EUCASS2023-916

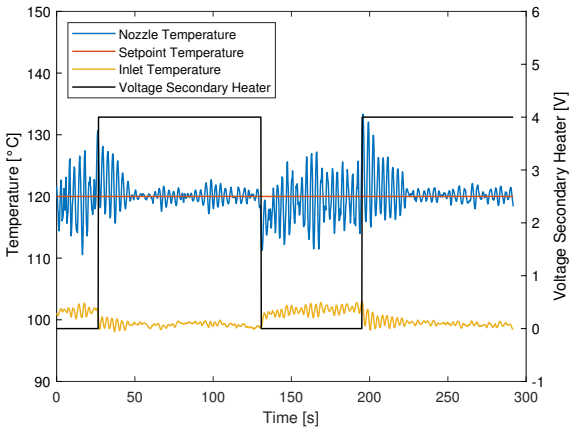

Figure 4: Effect of the secondary heater on the temperature.

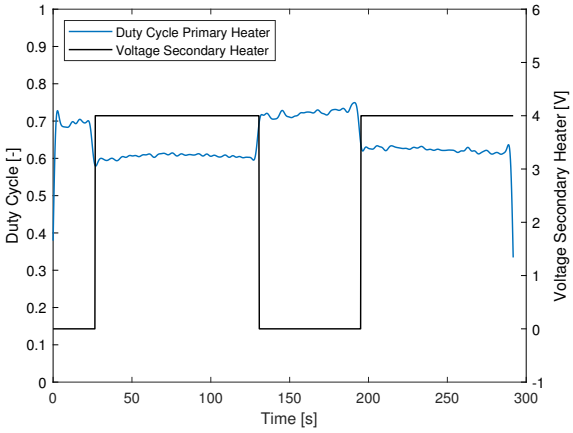

Figure 5: Effect of the secondary heater on the duty cycle.

by a customized adapter. Downstream of the boiling chamber, a larger (width: 3 mm) and longer (length: 8 mm) rectangular chamber accomplishes the flow vaporization and overheats the flow up to the desired temperature. Such a large modification of the cross-section is obtained through a divergent diffuser ($\alpha_{diff} = 30°$) placed between the microchannel-based boiling chamber and the rectangular overheating chamber. Finally, according to the reduced range of the mass flow rate, the throat section of the convergent-divergent micronozzle has been reduced from the original 150 µm to 25 µm.

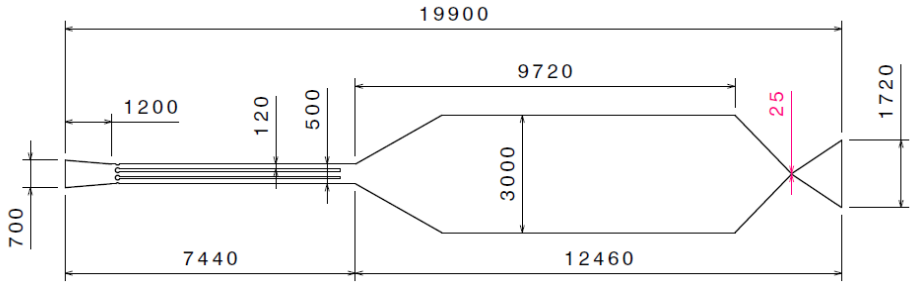

Figure 6: Sketch of the planar geometry of the new design with quotations (units: µm).

The microelectronics embedded in the new device has been simplified too. As shown in Figure 7(a), two microheaters have been integrated as follows. The main heater (thickness: 500 µm (denoted by the blue region) is deposited on the bottom of the silicon substrate in correspondance of the boiling chamber, while the secondary heater (thickness: 300 µm) is deposited on the glass substrate in direct contact with the flow. Finally, two RTDs are placed at the entrance and the exit of the boiling chamber, and a third one is located at the micronozzle entrance; one larger void fraction sensor (co-planar wave guide type as in the original design) has been installed at the microchannel exit (see Figure 7(b)).

The logic of splitting the overall heating process in two steps is due to the huge modification of the flow properties. In particular, the high density ratio makes impossible to use the same geometry for an efficient heat transfer from solid to the flow. The parallel microchannel geometry is convenient only when the fluid is enough liquid thanks to the increased heating surface, but when the vapor quality approaches to 1 and the flow is fully vaporized, a cross-section enlargement is required to slow down the flow and increase the residence time. This significantly reduces the required wall temperature for a given enthalpy rise, with a colder device and a more isoentropic and efficient heat transfer process as benefits.

This is clearly evinced by the numerical predictions in Figures 8 and 9, which refers to the same operating conditions (mass flow rate: $\dot{m} = 1.27 \times 10^{-6}$ kg/s; desired fluid temperature at the micronozzle entrance: $T_{fluid,exit} = 540$ K). At the exit of the microchannels region, the flow velocity drop down (Fig. 8(b)) from about 14 m/s to about 2 m/s, the vapor quality is 0.92 (blue solid line in Fig. 9(b)) and the wall temperature (red dash-dotted line in Fig. 9(a)) approaches the ultimate temperature of the device 573 K (black dash line in Fig. 9(a)).

As reported in Table 3 (second column), the heating power spent by the main heater is $P_{MH} = 3.10$ W. However,

DOI: 10.13009/EUCASS2023-916

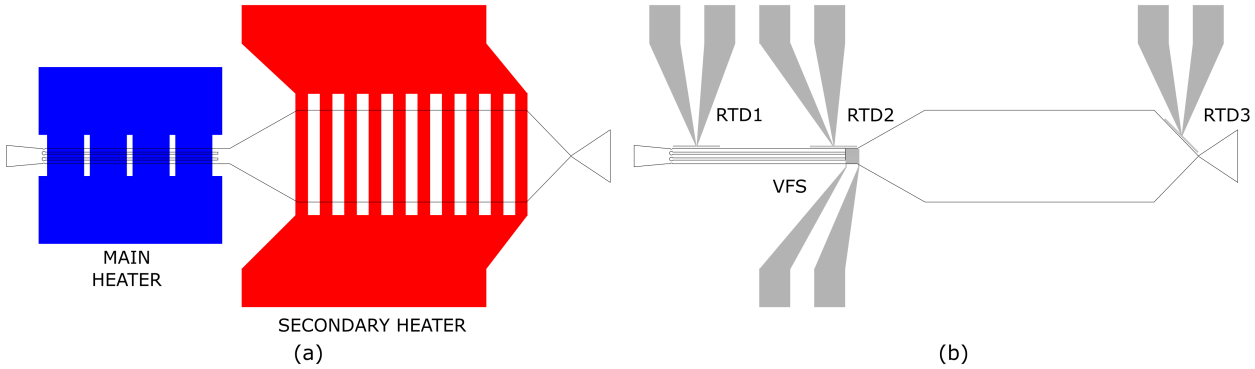

Figure 7: New VLM design: configuration of embedded microelectronics: (a) heating system; (b) temperature and void fraction sensing.

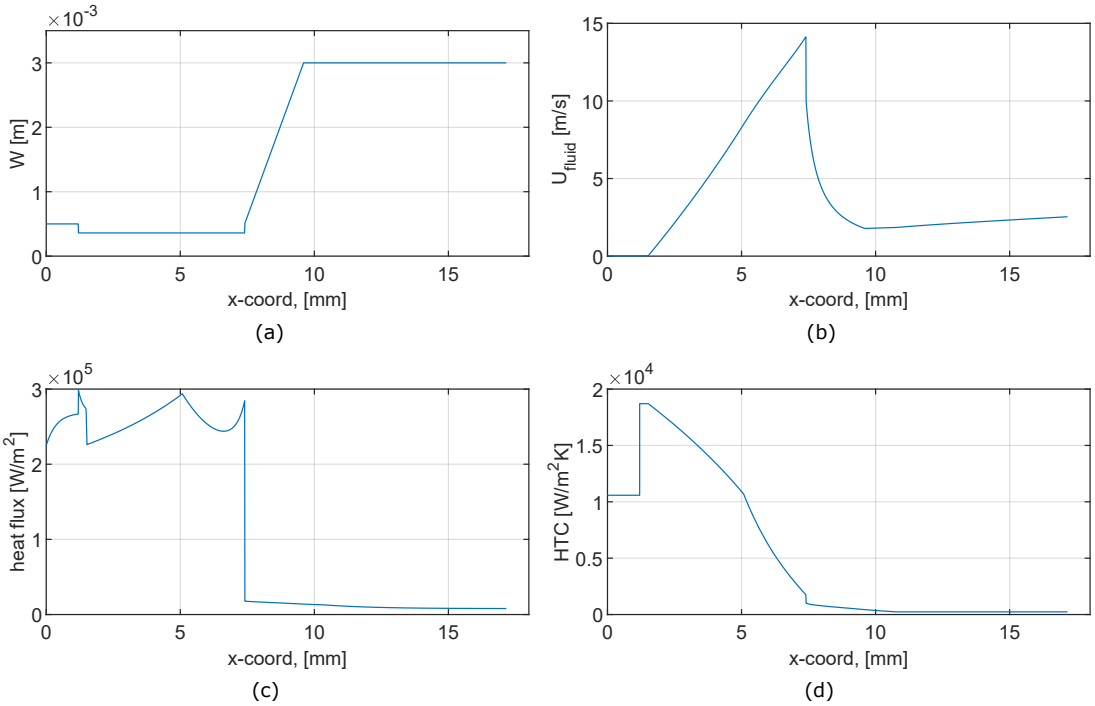

Figure 8: Numerical prediction of the two-phase flow with the new design: (a) spatial profile of the effective cross-section width W; (b) flow velocity U_{fluid}; (c) local heat flux; (d) heat transfer coefficient HTC.

Table 3: Numerical assessment of the dual heating and comparisons.

	$x_{vap,c}$ [-]		
	0.75	**0.92**	**0.94**
$T_{wall,max}$ [K]	616.0	573.8	606.5
$(T_{wall} - T_{fluid})_{exit}$ [K]	70.1	33.8	30.5
P_{PH} [W]	2.63	3.10	3.15
P_{SH} [W]	1.06	0.59	0.54
P_{tot} [W]	3.69	3.69	3.69
F [mN]	1.47	1.47	1.47
I_{sp} [s]	118	118	118

DOI: 10.13009/EUCASS2023-916

in the overheating chamber the heating power used to accomplish vaporization and reach the desired fluid temperature is only $P_{SH} = 0.59\,\mathrm{W}$. In such a way, the local heat flux reduces (see Fig. 8(c))), minimizing the required wall temperature together with the increased residence time. This allows to compensate the significant drop of the heat transfer coefficient (see Fig. 8(d)).

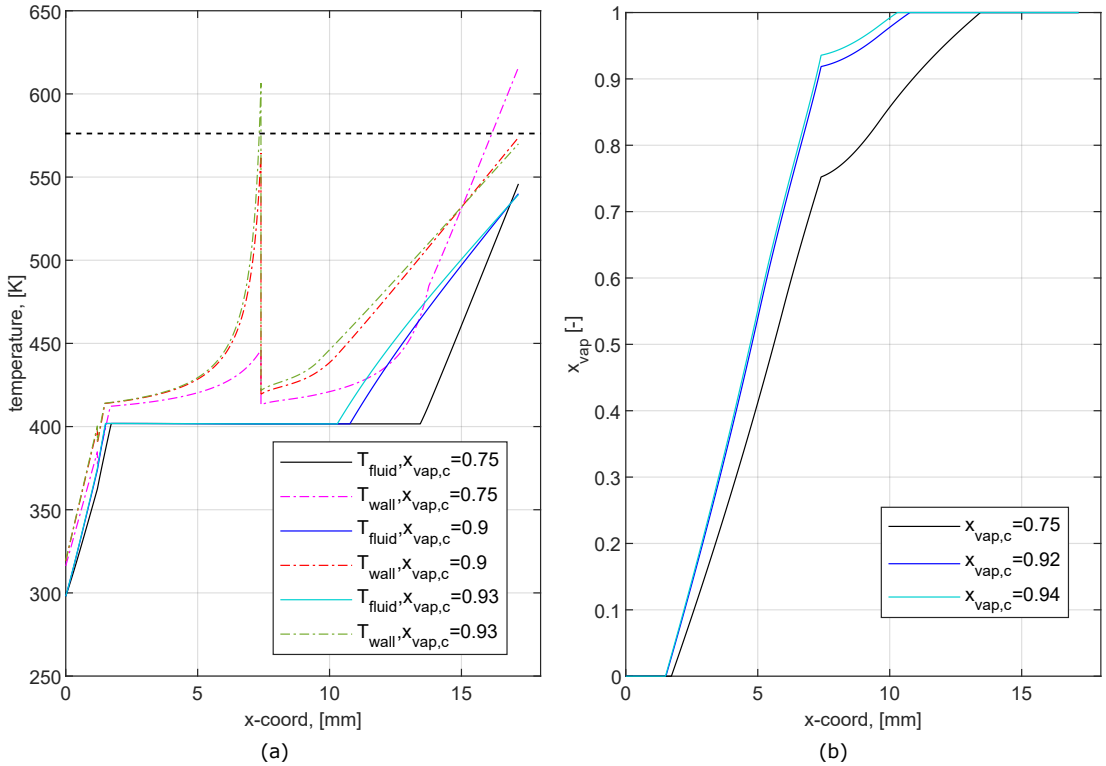

Figure 9: Numerical assessment of the dual heating as a function of the vapor quality at the microchannels exit $x_{vap,c}$: (a) wall (T_{wall}) and fluid (T_{fluid}) temperatures; (b) vapor quality x_{vap}.

However, there is an optimum in unbalancing the heating power between the primary heater and the secondary heater. This is also shown in Figure 9, where three void fraction conditions at the boiling chamber exit are compared, i.e. $x_{vap,c} = 0.75$, $x_{vap,c} = 0.92$ and $x_{vap,c} = 0.94$. By keeping constant the total heating power (see Tab. 3), the propulsive performance are also preserved ($F = 1.47\,\mathrm{mN}$ and $I_{sp} = 118\,\mathrm{s}$). However, by reducing the power applied to the primary heater and increasing the power applied to the secondary heater, the maximum wall temperature overcome the ultimate temperature during the overheating process; in the same way, by weakly increasing the power applied to the primary heater and reducing the power applied to the secondary heater, the maximum wall temperature overcome the ultimate temperature during the boiling process. This means that the vapor quality at the boiling chamber exit $x_{vap,c}$ must be controlled in the range 0.75 and 0.94 to avoid unfeasible thermal stresses and the device burnout, and ensure the device safety.

Finally, the effect of the desired temperature on the propulsive performance has been assessed. To this purpose, two different desired fluid temperatures have been considered, i.e., $T_{fluid,exit} = 540\,\mathrm{K}$ and $T_{fluid,exit} = 450\,\mathrm{K}$, while keeping constant the mass flow rate at $\dot{m} = 1.27 \times 10^{-6}\,\mathrm{kg/s}$ and $x_{vap,c} = 0.92$. As shown in Figure 10, the thermal behavior of the device (both walls and fluid) is similar, with lower temperatures at $T_{fluid,exit} = 450\,\mathrm{K}$ but same ($T_{wall} - T_{fluid}$). Furthermore, as expected the thrust force reduces to $F = 1.33\,\mathrm{mN}$; however, the specific impulse reduces too ($I_{sp} = 107\,\mathrm{s}$), denoting a less efficient operating conditions. This result outlines that a temperature-based thrust control is a suitable alternative with respect to a pressure-based thrust control; in fact, it is faster and more local, producing benefits in flow boiling instability control, as previously shown in Section 3.1.

4. Concluding remarks and future steps

A water-fed microfabricated vaporizing liquid microthruster has been designed and fabricated. In the present work, a new design is proposed to enhance the safety and efficiency of high-energy transfer from solid walls to fluid. A quasi-1D steady-state numerical model has been developed to solve the flow into the VLM at constant heat flux boundary

DOI: 10.13009/EUCASS2023-916

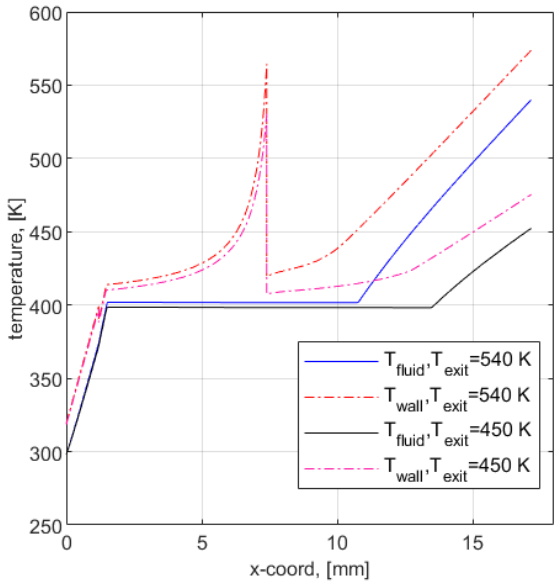

Figure 10: Numerical assessment of the dual heating: wall (T_{wall}) and fluid (T_{fluid}) temperatures as a function of the desired fluid temperature at the heating chamber exit T_{exit}.

conditions, allowing for a preliminary performance assessment of dual heating control. Furthermore, an experimental assessment of the heat transfer process on a real device undergoing dual heating control is provided, and the most relevant insights are discussed together with the numerical analysis.

Experiments carried out using devices with the original design have confirmed the feasibility of the secondary heating system, as well as the capability of the secondary heating in hindering the temperature oscillations and stabilize the flow boiling at the inlet chamber keeping colder (and safer) the device. The numerical assessment of the new configuration proves the existence of an optimum in unbalancing the heating power between the primary heater and the secondary heater: in this regard, the vapor quality at the boiling chamber exit must be controlled in the range 0.75 and 0.94 to avoid unfeasible thermal stresses and the device burnout, and ensure the device safety.

Future research will perform a comprehensive experimental investigation of the new design of VLM undergoing actively controlled pulsed dual heating. To this purpose, the void fraction sensor will be integrated in the feedback control together with the embedded temperature micro-sensors.

5. Acknowledgments

The authors gratefully acknowledge the financial support of the European Space Agency from the Open Space Innovation Program (OSIP) - Open Discovery Ideas, grant No. 4000 135973/21/NL/GLC/my. Special acknowledgement also to the technical staff of CNR-IMM C. Martucci, A. Campa, P. Cret'i, E. Melissano, F. Casino; to H. Van Eyken and T. Heskens (KU Leuven) for their precious support during the research activities.

References

[1] Juergen Mueller, William Tang, Andrew Wallace, Russel Lawton, Wen Li, David Bame, and Indrani Chakraborty. Design, analysis and fabrication of a vaporizing liquid micro-thruster. In *33rd Joint Propulsion Conference and Exhibit*, page 3054, 1997.

[2] Juergen Mueller, David Bame, Indrani Chakraborty, Andrew Wallace, William Tang, and Russell Lawton. Proof-of-concept demonstration of a vaporizing liquid micro-thruster. In *34th AIAA/ASME/SAE/ASEE Joint Propulsion Conference and Exhibit*, page 3924, 1998.

[3] Juergen Mueller, Indrani Chakraborty, David Bame, and William Tang. Vaporizing liquid microthruster concept: Preliminary results of initial feasibility studies. *Micropropulsion for small spacecraft, Reston, VA, American Institute of Aeronautics and Astronautics, Inc.(Progress in Astronautics and Aeronautics.*, 187:215–230, 2000.

DOI: 10.13009/EUCASS2023-916

[4] Y. Gao, Y. F. Ma, and J. T. Liu. A review of the vaporizing liquid microthruster technology. In *2014 ISFMFE - 6th International Symposium on Fluid Machinery and Fluid Engineering*, pages 1–3, 2014.

[5] E.V Mukerjee, A.P Wallace, K.Y Yan, D.W Howard, R.L Smith, and S.D Collins. Vaporizing liquid microthruster. *Sensors and Actuators A: Physical*, 83(1):231 – 236, 2000.

[6] DK Maurya, S Das, and SK Lahiri. Silicon mems vaporizing liquid microthruster with internal microheater. *Journal of Micromechanics and Microengineering*, 15(5):966, 2005.

[7] Pijus Kundu, Tarun Kanti Bhattacharyya, and Soumen Das. Design, fabrication and performance evaluation of a vaporizing liquid microthruster. *Journal of Micromechanics and Microengineering*, 22(2):025016, 2012.

[8] X.Y. Ye, F. Tang, H.Q. Ding, and Z.Y. Zhou. Study of a vaporizing water micro-thruster. *Sensors and Actuators, A: Physical*, 89(1-2):159–165, 2001.

[9] M.A.C. Silva, D.C. Guerrieri, H. van Zeijl, A. Cervone, and E. Gill. Vaporizing liquid microthrusters with integrated heaters and temperature measurement. *Sensors and Actuators, A: Physical*, 265:261–274, 2017.

[10] Bendong Liu, Xinrui Li, Xu Yang, Jiahui Yang, Yuezong Wang, Desheng Li, and Guohua Gao. A new vaporizing liquid microthruster with planar induction heating. *Sensors and Actuators A: Physical*, 308:112010, 2020.

[11] Bendong Liu, Xu Yang, and Yuezong Wang. A tubular vaporizing liquid micro-thruster with induction heating. *Heat and Mass Transfer*, 56:2035–2043, 2020.

[12] Akshay Sharma, Narendra Dev, and Susmita Dash. Capillary-fed evaporative microthruster for nano/microsatellites. In *AIAA SCITECH 2022 Forum*, page 0240, 2022.

[13] Steven M Pugia, Ryan J Clay, Matthew F Fuehne, Margaret M Linker, Noah C Franks, Benjamin Davis, and Katherine L Fowee. Liquid water micropropulsion system for small satellites. In *AIAA Scitech 2019 Forum*, page 0153, 2019.

[14] Steven Pugia, Anthony Cofer, and Alina Alexeenko. Characterization of film-evaporating microcapillaries for water-based microthrusters. *Acta Astronautica*, 196:442–458, 2022.

[15] Daduí C Guerrieri, Marsil AC Silva, Angelo Cervone, and Eberhard Gill. Selection and characterization of green propellants for micro-resistojets. *Journal of Heat Transfer*, 139(10):102001, 2017.

[16] Donato Fontanarosa, Luca Francioso, Maria Grazia De Giorgi, and Maria Rosaria Vetrano. Mems vaporazing liquid microthruster: A comprehensive review. *Applied Sciences*, 11(19), 2021.

[17] C.-C. Chen, C.-W. Liu, H.-C. Kan, L.-H. Hu, G.-S. Chang, M.-C. Cheng, and B.-T. Dai. Simulation and experiment research on vaporizing liquid micro-thruster. *Sensors and Actuators, A: Physical*, 157(1):140–149, 2010.

[18] J.W. Cen and J.L. Xu. Performance evaluation and flow visualization of a mems based vaporizing liquid microthruster. *Acta Astronautica*, 67(3-4):468–482, 2010.

[19] Pok-Wang Kwan, Xun Huang, and Xin Zhang. Design and testing of a microelectromechanical-system-based high heat flux vaporizing liquid microthruster. *Acta Astronautica*, 170:719–734, 2020.

[20] Donato Fontanarosa, Chiara De Pascali, Maria Grazia De Giorgi, P. Siciliano, Antonio Ficarella, and Luca Francioso. Fabrication and embedded sensors characterization of a micromachined water-propellant vaporizing liquid microthruster. *Applied Thermal Engineering*, 188:116625, 2021.

[21] D. Fontanarosa, L. Francioso, M.G. De Giorgi, C. De Pascali, A. Ficarella, and M.R. Vetrano. Flow regime characterization of a silicon-based vaporizing liquid microthruster. *Acta Astronautica*, 193:691–703, 2022.

[22] Donato Fontanarosa, Dries Van Langenhove, Angelica Maria Toscano, Maria Grazia De Giorgi, Frederik Mertens, Maria Assunta Signore, Maria Rosaria Vetrano, Johan Steelant, and Luca Francioso. Optimized vaporization in liquid-fed microresistojets using pulsed heating. In *73rd International Astronautical Congress (IAC)*. International Astronautical Federation (IAF), 2022.

[23] M.G. De Giorgi and D. Fontanarosa. A novel quasi-one-dimensional model for performance estimation of a vaporizing liquid microthruster. *Aerospace Science and Technology*, 84:1020–1034, 2019.

DOI: 10.13009/EUCASS2023-916

[24] Theodore L Bergman and Frank P Incropera. *Introduction to heat transfer*. John Wiley & Sons, 2011.

[25] Ian H. Bell, Jorrit Wronski, Sylvain Quoilin, and Vincent Lemort. Pure and pseudo-pure fluid thermophysical property evaluation and the open-source thermophysical property library coolprop. *Industrial & Engineering Chemistry Research*, 53(6):2498–2508, 2014.

[26] C.B. Tibiriçá, D.M. Rocha, Jr. Sueth, I.L.S., G. Bochio, G.K.K. Shimizu, M.C. Barbosa, and S.D.S. Ferreira. A complete set of simple and optimized correlations for microchannel flow boiling and two-phase flow applications. *Applied Thermal Engineering*, 126:774–795, 2017.

[27] George P Sutton and Oscar Biblarz. *Rocket propulsion elements*. John Wiley & Sons, 2016.

[28] N.M. Kuluva and G.A. Hosack. Supersonic nozzle discharge coefficients at low reynolds numbers. *AIAA Journal*, 9(9):1876–1879, 1971.

[29] E.I. Sokolov and M.V. Chernyshov. Optimization of micronozzle performance at zero ambient pressure. *Acta Astronautica*, 2017.

[30] David L Whitfield. Integral solution of compressible turbulent boundary layers using improved velocity profiles. Technical report, ARNOLD ENGINEERING DEVELOPMENT CENTER ARNOLD AFB TN, 1978.

[31] A Cengel Yunus and John M Cimbala. *Fluid mechanics fundamentals and applications*, volume 185201. International Edition, McGraw Hill Publication, 2006.

[32] Adrian Bejan and Allan D Kraus. *Heat transfer handbook*, volume 1. John Wiley & Sons, 2003.